Numerical Simulation of the Rainfall Infiltration on Unsaturated Soil Slope Considering a Seepage Flow

S.Kimoto [1], F.Oka[2] and E.Garcia[3]
[1,2]*Department of Civil and Earth Resources Engineering, Kyoto University, Kyoto, Japan*
[3]*Escuela Ambiental, Universidad de Antioquia UdeA, Medellín, Colombia*
[1]*E-mail*: kimoto.sayuri.6u@kyoto-u.ac.jp
[2]*E-mail*: oka.fusao.38x@st.kyoto-u.ac.jp
[3]*E-mail*: egarcia@udea.edu.co

ABSTRACT: Frequent failures of river embankments have occurred in the world due to heavy rains. Heavy rainfalls bring about an increase of the ground water level within the soil as well as a rise in the water level of the rivers. As a result, embankments have been failed due to the rainfall infiltration and the generation of seepage flow. A series of two-dimensional numerical analyses of river embankments are carried out using a seepage-deformation coupled method for unsaturated soil. The mechanism of the surface deformation and the strain localization on these soil structures are discussed mainly with respect to the water permeability of the soils. Results obtained by the simulations show that the deformation of the embankments significantly depends on the water permeability of the soil and it is localized on the slope surface at the river sides. The larger the saturated water permeability of the soil, the larger the velocity of the seepage flow and the larger the deformation on the surface of the river embankments. Additionally, numerical simulations of a field experiment are used to show that, the method adopted here, can effectively be used to study the practical seepage deformation coupled problems on unsaturated soils.

1. INTRODUCTION

In recent years, frequent failures of river embankments have occurred in the world due to heavy rains and typhoons. Heavy rainfalls bring about a rise in the water level of the rivers as well as a rise in the ground water level within the river embankments. As a result, river embankments have been failed due to the rainfall infiltration and the generation of seepage flow. In addition, sometimes the upper parts of the river levees are connected to the surrounding mountains being exposed to the continuous seepage flow from the hilly areas. This, in turn, increases the pore water pressures within the river embankment leading to the degradation of the material (e.g., seepage-induced erosion). This deformation could trigger the progressive failure of the river embankments endangering the nearby structures.

Many researchers have reported on the embankment and slope failure due to the rainfall infiltration (e.g., Yoshida et al., 1991; Au, 1998; Alonso et al., 2003; Yamagishi et al., 2004, 2005; Matsushi et al., 2006; Chen et al., 2006; Nakata et al., 2010;); similarly, some studies have addressed the effect of the rainfall in infiltration on the slope stability from the point of view of the statistical approach (e.g. Au, 1993; Okada and Sugiyama, 1994).

Failure of embankments has also been studied from the numerical approach, several researchers have been implementing numerical solutions to analyse the effect of the hydraulic characteristics on the instability of unsaturated slopes (e.g. Ng and Shi, 1998; Tsaparas et al., 2002, Cai and Ugai, 2004; Rahardjo et al., 2007). In these formulations, the effects of the rainfall infiltration on the generation of the pore water pressure and the instability of the slope are generally evaluated by a seepage analysis using the finite element method and followed by the slope stability analysis; thus, the study of the coupling of the deformation and the transient flow is disregarded. However, it is also possible to use numerical methods that can simultaneously consider the unsaturated seepage flow and the deformation of soil structures to study the infiltration processes (Cho and Lee, 2001; Alonso et al., 2003; Ehlers et al., 2004; Ye et al., 2005; Oka et al., 2009, Oka and Kimoto,2012)).

In this paper a study to clarify the effect of the rainfall infiltration considering seepage flow on the deformation of unsaturated river embankments is presented. To do that, two-dimensional numerical analyses have been performed for two river embankments. The first case study, namely Seta River, corresponds to a three layered river embankment which is subjected to both, the effect of the rainfall infiltration and the seepage flow from the mountain side. In the simulation, a rainfall record measured at the Seta River (Shiga Prefecture, Japan) and the variation of the water level measured at the right side of the embankment are used for the analyses, whereas the water level of the river is considered constant. In the Seta River case, the study of the effect of different water permeabilities for the upper layer on the seepage flow velocity and its effect on the surface deformation are emphasized. Furthermore, the effects of horizontal drains and the degree of compaction on the generation of deformation are investigated. The second case study is a controlled experiment performed in the field, namely S River, and it corresponds to a river dike embankment used to protect the urban areas from the flooding triggered by the rainfall accumulation and the increase of the water level of the rivers. The analyses performed for this case are also based on the variation of the saturated water permeabilities of the soil layers. Rainfall infiltration is applied on the surface of the dike while the water level is increased and decreased to observe the effect of the seepage flow on the generation of pore water pressure and on the deformation of the embankment. The results obtained by the numerical analyses for the pore water pressure are compared with the existing measured field data.

The numerical analyses have been carried out using a seepage-deformation coupled method for unsaturated soil. Constitutive and hydraulic parameters that represent the soils found in the Seta River and S River embankments are employed in the simulations. From the numerical results, it was observed that the deformation of the embankment significantly depends on the water permeability of the soil and it is localized on the slope surface at the river side. The larger the saturated water permeability of the soil, the larger the velocity of the seepage flow and the larger the deformation on the surface of the river embankment.

2. MULTIPHASE COUPLED ELASTO-VISCOPLASTIC FORMULATION

2.1 Governing Equations

Unsaturated material is assumed to be composed of three phases, namely, solid (*S*), water (*W*), and air (*G*), which are continuously distributed throughout space. Total volume V and volume of the voids V^V are obtained from the sum of the partial volumes of the constituents, namely,

$$V = V^S + V^W + V^G \tag{1}$$

$$V^V = V^W + V^G \tag{2}$$

Volume fraction n^α (α= *S*, *W*, and *G*) is defined as the ratio of the specific volume element with respect to the total volume, namely,

$$n^\alpha = \frac{V^\alpha}{V} \tag{3}$$

$$n^S + n^W + n^G = 1 \tag{4}$$

The porosity, *n*, is written as

$$n = \frac{V^V}{V} = \frac{V - V^S}{V} = 1 - n^S \tag{5}$$

In addition, water saturation *s* is required in the model, namely,

$$s = \frac{V^W}{V^V} = \frac{V^W}{V^W + V^G} = \frac{n^W}{n} \tag{6}$$

2.1.1 Skeleton Stress

The behaviour of a material is described within the framework of a macroscopic continuum mechanical approach through the use of the theory of porous media (Boer, 1998; Ehlers et al., 2004; Kimoto et al., 2007, 2010). The theory is considered to be a generalization of Biot's two-phase mixture theory for saturated soil (Biot, 1941, 1962). Terzaghi (1943) defined the effective stress for water-saturated soil. In the case of unsaturated soil, however, the effective stress needs to be redefined in order to include a third phase, namely, the air phase. This phase is considered to be compressible. In the present formulation, skeleton stress tensor σ'_{ij} is defined and then used for the stress variable in the constitutive relation for the soil particles (Kimoto et al., 2007); Jommi (2000) defined it as the average soil skeleton stress.

The partial stress values for the fluid phase have been expressed as

$$\sigma_{ij}^W = -n^W P^W \delta_{ij} \tag{7}$$

$$\sigma_{ij}^G = -n^G P^G \delta_{ij} \tag{8}$$

where P^W and P^G are the pore water pressure and the pore air pressure, respectively.

The partial stress tensor for the solid phase, σ^S_{ij}, can be expressed by an analogy with the water-saturated phase as

$$\sigma_{ij}^S = \sigma'_{ij} - n^S P^F \delta_{ij} \tag{9}$$

where P^F is the average pore pressure. Total stress tensor σ_{ij} is obtained from the sum of the partial stress values, namely,

$$\sigma_{ij} = \sigma_{ij}^S + \sigma_{ij}^W + \sigma_{ij}^G \qquad S\text{=Solid, } W\text{=Water, } G\text{=Air.} \tag{10}$$

Substituting Equations (7) to (9) into Equation (10), and considering Equations (4) to (6), we have

$$\sigma'_{ij} = \sigma_{ij} + P^F \delta_{ij} \tag{11}$$

where σ'_{ij} is the skeleton stress, which is used as the basic stress variable in the model for unsaturated soil. In Equation (11), the average pore pressure (Jommi, 2000) is given by

$$P^F = sP^W + (1-s)P^G \tag{12}$$

2.1.2 Mass Conservation Law

The conservation of mass for the soil, the water, and the air phases is given by the following equations:

$$\frac{D^\alpha}{Dt}\left(n^\alpha \rho_\alpha\right) + n^\alpha \rho_\alpha v^\alpha_{i,i} = 0 \qquad \alpha = S, W, G \tag{13}$$

in which ρ_α and v_i^α are the material density and the velocity of each phase, respectively. D^α/Dt denotes the material time derivative following the mass of phase α.

Supposing that the soil particles and water are incompressible, namely, $\dot{\rho}_S = 0$ and $\dot{\rho}_W = 0$, the conservation laws of Equation (13) yield

$$\dot{n}^S \rho_S + n^S \rho_S v^S_{i,i} = 0 \tag{14}$$

$$\dot{n}^W \rho_W + n^W \rho_W v^W_{i,i} = 0 \tag{15}$$

$$\dot{n}^G \rho_G + n^G \dot{\rho}_G + n^G \rho_G v^G_{i,i} = 0 \tag{16}$$

where the superimposed dot denotes the material time derivative following particles of each phase, respectively.

Considering Equations (5) and (6), Equations (14) to (16) provide

$$-\dot{n}\rho_S + (1-n)\rho_S v^S_{i,i} = 0 \tag{17}$$

$$\dot{n}\, s\, \rho_W + n\, \dot{s}\, \rho_W + n\, s\, \rho_W v^W_{i,i} = 0 \tag{18}$$

$$\dot{n}(1-s)\rho_G - n\dot{s}\rho_G + n(1-s)\dot{\rho}_G + n(1-s)\rho_G v^G_{i,i} = 0 \tag{19}$$

The apparent velocity or flux vector V_i^β of water and air, with respect to the solid phase, is defined as

$$V_i^\beta = n^\beta\left(v_i^\beta - v_i^S\right) \qquad \beta = W, G \tag{20}$$

Multiplying Equation (17) by $s(\rho_W/\rho_S)$, adding Equation (18), and considering Equation (20), the continuity equation for the water phase can be obtained as

$$s v^S_{i,i} + n\dot{s} = -V^W_{i,i} \tag{21}$$

Similarly, multiplying Equation (17) by $(1\text{-}s)\rho_G/\rho_S$, adding Equation (19), and considering Equation (20), the continuity equation for the air phase can be obtained as

$$(1-s)v^S_{i,i} - n\dot{s} + n(1-s)\frac{\dot{\rho}_G}{\rho_G} = -V^G_{i,i} \tag{22}$$

To describe the changes in air density, the equation for ideal gas is used, i.e.,

$$\rho^G = \frac{MP^G}{R\theta} \tag{23}$$

$$\dot{\rho}^G = \frac{M}{R}\left(\frac{\dot{P}^G}{\theta} - \frac{P^G\dot{\theta}}{\theta^2}\right) \tag{24}$$

in which M is the molecular weight of the gas, R is the gas constant, and θ is the temperature.

2.1.3 Conservation of Momentum

The momentum balance equations for the three phases are given by

$$n^\alpha \rho_\alpha \dot{v}_i^\alpha = \sigma_{ji,j}^\alpha + \rho_\alpha n^\alpha \overline{F}_i + \sum_\gamma D^{\alpha\gamma}\left(v_i^\alpha - v_i^\gamma\right) \quad \alpha,\gamma = S,W,G \tag{25}$$

in which $\overline{F}_i$ is the gravitational force per unit mass and $D^{\alpha\gamma}$ ($D^{\alpha\gamma}$=$D^{\gamma\alpha}$) are the parameters which describe the interaction between phases α and γ, which is defined as

$$D^{WS} = -\frac{\left(n^W\right)^2 \rho_W g}{k^W} \qquad D^{GS} = -\frac{\left(n^G\right)^2 \rho_G g}{k^G} \tag{26}$$

in which k^W and k^G are the permeability coefficients for the water phase and the air phase, respectively.

Disregarding the acceleration and the interaction between air and water, the momentum balance equations for the three phases are obtained as

$$\sigma'_{ji,j} - \left(n^S P^F\right)_{,i} + \rho_S n^S \overline{F}_i + D^{SW}\left(v_i^S - v_i^W\right) + D^{SG}\left(v_i^S - v_i^G\right) = 0 \tag{27}$$

$$-\left(n^W P^W\right)_{,i} + \rho_W n^W \overline{F}_i + D^{WS}\left(v_i^W - v_i^S\right) = 0 \tag{28}$$

$$-\left(n^G P^G\right)_{,i} + \rho_G n^G \overline{F}_i + D^{GS}\left(v_i^G - v_i^S\right) = 0 \tag{29}$$

Supposing that the distribution of porosity is sufficiently smooth and using Equation (26), Darcy's laws for the water and the air phases are obtained from Equations (28) and (29), respectively, as

$$V_i^W = n^W\left(v_i^W - v_i^S\right) = -\frac{k^W}{\rho_W g}\left(P_{,i}^W - \rho_W \overline{F}_i\right) \tag{30}$$

$$V_i^G = n^G\left(v_i^G - v_i^S\right) = -\frac{k^G}{\rho_G g}\left(P_{,i}^G - \rho_G \overline{F}_i\right) \tag{31}$$

The sum of Equations (27) to (29) leads to the equilibrium equation for the whole mixture

$$\sigma_{ji,j} + \rho \overline{F}_i = 0 \tag{32}$$

where ρ is the density of the mixture.

2.2 Constitutive Equations for the Soil

2.2.1 Headings Soil Water Characteristic Curve

The relation between suction P^C=P^G-P^W and effective saturation s_{re} is given by the equation proposed by van Genuchten (1980) as

$$s_{re} = \left\{1 + \left(\alpha P^C\right)^{n'}\right\}^{-m} \tag{33}$$

$$s_{re} = \frac{s - s_{\min}}{s_{\max} - s_{\min}} \tag{34}$$

in which α, n', and m are material parameters, and the relation $m=1-1/n'$ is assumed. s_{max} and s_{min} are the maximum and the minimum limiting values of saturation, respectively.

The effects of the degree of saturation on permeability for water and air are assumed as

$$k^W = k_s^W s^a\left\{1 - \left(1 - s^{\frac{1}{m}}\right)^{n'}\right\} \qquad k^G = k_s^G\left(1-s\right)^b\left\{1 - \left(s^{\frac{1}{m}}\right)^{n'}\right\} \tag{35}$$

where a and b are the material parameters, and m and n' are the parameters in the van Genuchten equation. k^W_s is the coefficient of permeability for water under saturated conditions and k^G_s is the coefficient of permeability for air under fully dry conditions.

2.2.2 Elasto-viscoplastic Model for Unsaturated Soil

An elasto-viscoplastic model, based on the overstress-type of viscoplastic theory with soil structure degradation for saturated soil (Kimoto and Oka, 2005), has been extended to unsaturated soils using the skeleton stress and the suction effect in the constitutive model (Oka et al., 2006).

It is assumed that total strain rate tensor consists of elastic strain rate tensor and viscoplastic strain rate tensor as

$$\dot{\varepsilon}_{ij} = \dot{\varepsilon}_{ij}^e + \dot{\varepsilon}_{ij}^{vp} \tag{36}$$

The elastic strain rate tensor is given by a generalized Hooke type of law, i.e.,

$$\dot{\varepsilon}_{ij}^e = \frac{1}{2G}\dot{S}_{ij} + \frac{\kappa}{3(1+e)}\frac{\dot{\sigma}'_m}{\sigma'_m}\delta_{ij} \tag{37}$$

where S_{ij} is the deviatoric stress tensor, σ'_m is the mean skeleton stress, G is the elastic shear coefficient, e is the void ratio, κ is the swelling index, and the superimposed dot denotes the material time derivative following particles of solid phase.

In this model, it is assumed that there is an overconsolidation (OC) boundary surface that delineates the normally consolidated (NC) region, f_b>=0, and the overconsolidated region (OC), f_b<0. Overconsolidation boundary surface f_b and static yield function f_y are defined as follows:

$$f_b = \overline{\eta}^*_{(0)} + M^*_m \ln(\sigma'_m / \sigma'_{mb}) = 0 \tag{38}$$

$$f_y = \overline{\eta}^*_{(0)} + \tilde{M}^* \ln(\sigma'_m / \sigma'^{(s)}_{my}) = 0 \tag{39}$$

$$\overline{\eta}^*_{(0)} = \left\{\left(\eta^*_{ij} - \eta^*_{ij(0)}\right)\left(\eta^*_{ij} - \eta^*_{ij(0)}\right)\right\}^{\frac{1}{2}} \qquad \eta^*_{ij} = \frac{S_{ij}}{\sigma'_m} \tag{40}$$

where M^*_m is the value of η^*=(η^*_{ij} η^*_{ij})$^{1/2}$ when the volumetric strain increment changes from contraction to dilation, which is equal to ratio M^*_f at the critical state, σ'_{mb} is the hardening parameter, and $\sigma'^{(s)}_{my}$ is the static hardening parameter. The effect of the unsaturated soil is incorporated for both boundaries as

$$\sigma'_{mb} = \sigma'_{ma}\exp\left(\frac{1+e}{\lambda-\kappa}\varepsilon_{kk}^{vp}\right)\left[1 + S_I \exp\left\{-s_d\left(\frac{P_i^c}{P^c} - 1\right)\right\}\right] \tag{41}$$

$$\sigma'^{(s)}_{my} = \frac{\sigma'^{(s)}_{myi}}{\sigma'_{mai}} \sigma'_{ma} \exp\left(\frac{1+e}{\lambda-\kappa}\varepsilon^{vp}_{kk}\right)\left[1+S_I \exp\left\{-s_d\left(\frac{P^c_i}{P^c}-1\right)\right\}\right] \quad (42)$$

where ε^{vp}_{kk} is the viscoplastic volumetric strain, λ is the compression index, and e is the initial void ratio. P^C_i is the initial suction value, P^C is the present suction value, and S_I is the material parameter that denotes the strength ratio to the saturated soil when suction is P^C_i. S_d is the parameter which controls the rate of increase or decrease in strength. σ'_{ma} is a strain-softening parameter used to describe the degradation of the material caused by structural changes, namely,

$$\sigma'_{ma} = \sigma'_{maf} + (\sigma'_{mai} - \sigma'_{maf})\exp(-\beta z) \quad (43)$$

$$z = \int_0^t \dot{z} dt \qquad \dot{z} = \sqrt{\dot{\varepsilon}^{vp}_{ij}\dot{\varepsilon}^{vp}_{ij}} \quad (44)$$

in which σ'_{mai} and σ'_{maf} are the initial and the final values of σ'_{ma}, respectively, β is a material parameter which controls the rate of structural changes, and z is the accumulation of the second invariant of viscoplastic strain rate .

Details of the constitutive model with soil structure degradation are given by Kimoto and Oka (2005).

The viscoplastic potential surface is described as

$$f_p = \overline{\eta}^*_{(0)} + \tilde{M}^* \ln(\sigma'_m / \sigma'_{mp}) = 0 \quad (45)$$

where $\tilde{M}^*$ is assumed to be constant in the NC region and to vary with the current stress in the OC region as

$$\tilde{M}^* = \begin{cases} M^*_m & \text{NC Region} \\ -\dfrac{\sqrt{\eta^*_{ij}\eta^*_{ij}}}{\ln(\sigma'_m/\sigma'_{mc})} & \text{OC Region} \end{cases} \quad (46)$$

where M^*_m is the value of $\sqrt{\eta^*_{ij}\eta^*_{ij}}/\sigma'_m$ at the critical state, and σ'_{mc} denotes the mean skeleton stress at the intersection of the OC boundary surface and the σ'_m axis as

$$\sigma'_{mc} = \sigma'_{mb} \exp \frac{\sqrt{\eta^*_{ij(0)}\eta^*_{ij(0)}}}{M^*_m} \quad (47)$$

Finally, the viscoplastic strain rate tensor is given by the following equation when *fy>0*, which is based on Perzyna's type of viscoplastic theory as

$$\dot{\varepsilon}^{vp}_{ij} = C_{ijkl}\sigma'_m \exp\left\{m'\left(\overline{\eta}^*_{(0)} + \tilde{M}^* \ln\frac{\sigma'_m}{\sigma'_{mb}}\right)\right\}\frac{\partial f_p}{\partial \sigma'_{kl}}$$

$$C_{ijkl} = D\delta_{ij}\delta_{kl} + E(\delta_{ik}\delta_{jl} + \delta_{il}\delta_{jk}) \quad C_1 = 2E \quad C_2 = 3D + 2E \quad (48)$$

in which C_1 and C_2 are the viscoplastic parameters for the deviatoric and the volumetric components, respectively.

3. NUMERICAL ANALYSIS

In the following, a general description of the methodology and boundaries used for the numerical analysis of rainfall infiltration on unsaturated soil slopes are presented. In this formulation, an updated Lagrangian method with the objective Jaumann rate of Cauchy stress is adopted (Fung and Tong, 2001; Nemat-Nasser, 2004, Oka and Kimoto, 2012)). The independent variables are the pore water pressure (P^W), the pore air pressure (P^G), and the nodal velocity (u). In the finite element formulation, an eight-node quadrilateral element with a reduced Gaussian integration is used for the displacement, and four nodes are used for the pore water pressure and the pore air pressure. The backward finite difference method is used for the time discretization.

3.1 Case A: Seta River - Japan

The river embankment used for the study is located in Otsu city, Shiga prefecture, Japan. Figure 1 shows a sketch of the geomorphology of the study area of the Seta River embankment. As it is observed on the figure, the back of the embankment is surrounded by a hilly area. The embankment is located in a flat surface which is divided by small rivers that flow toward the Seta River. The study area was a farmland but nowadays has become a resident area. The soil investigation and the observation of the behaviour of the embankment at Seta River have shown that the water infiltration from the surrounding mountains has been permanent and it has a significant impact on the damage and degradation of the soil close to the embankment surface at the river side. Figure 2 depicts the mechanics of the water flow and the degradation of the soil surface at the river side of the embankment. The fluctuation of the water level of the river at Seta River site is within one meter in a year.

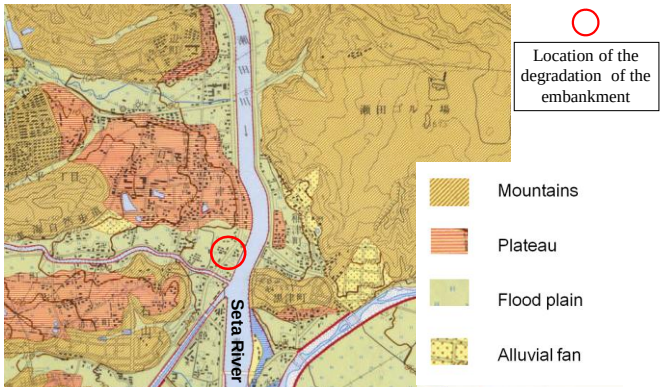

Figure 1 Geomorphology and location of the degradation of Seta River Embankment

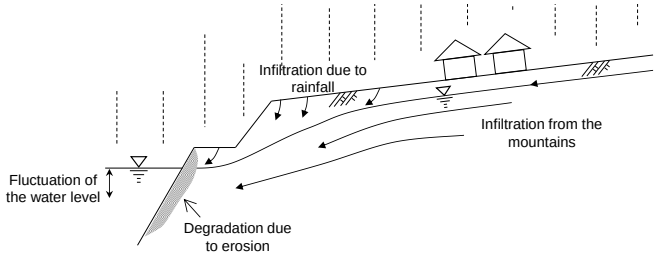

Figure 2 Mechanism of the water flow and degradation of the slope surface

Figure 3 shows the rainfall record at Seta River and the ground water level observations at the right side of the embankment (mountain side) from January 2009 to February 2010. This figure shows that the ground water level changes over the time and increases when the rainfalls are presented. This is an indication of the appearance of seepage flow induced by the rainfall infiltration.

The cross section and the boundary conditions for the simulation of the rainfall infiltration and seepage flow into the unsaturated river embankment are shown in Figure 4. The top surface of the river embankment has an inclination of 0.95°. The slopes of the embankment have gradients of 1V:1H at the upper part and 1V:3H at the middle of the embankment. For displacement, the embankment is fixed at the bottom in both horizontal and vertical directions; the lateral boundaries are fixed only in horizontal

direction. The initial negative pore water pressure distribution (suction) in the top sandy gravel layer is considered to be linear. The water level at the boundaries of the embankment is located at 21.2 m at the river side and at 24.3 m at the mountain side. The water level inside the embankment is linearly distributed according with the water levels at the river and mountain sides; its inclination is about 1.5°. The flux of air is allowed for the entire boundaries and the initial air pressure, P^G_i, is assumed to be zero. The boundary conditions for water flux are described in this manner: an impermeable boundary is assigned to the bottom or soil foundation; for the lateral sides of the embankment below the water levels, the boundary is considered permeable; above the water levels the boundaries are initially impermeable, but it changes to be permeable if the pore water pressure turns positive. In the case of rainfall, if the soil is unsaturated, a flow boundary is used on the slope surface and the whole water infiltrates into the soil; but, once the surface is saturated, a prescribed pore water pressure equal to zero is used on the surface; in this case, the incoming of water is controlled by the gradient of the matric suction inside the embankment. Thus, it is possible to control the volume of the water that comes into the soil and the excess of water is dissipated as runoff.

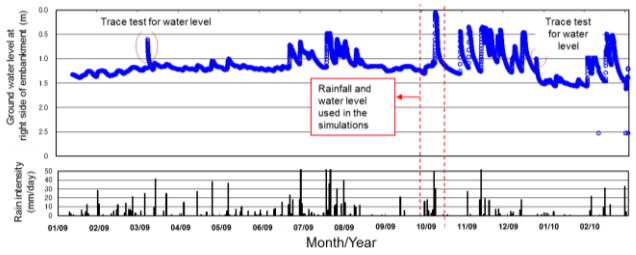

Figure 3 Rainfall and water level data from January 2009 to February 2010

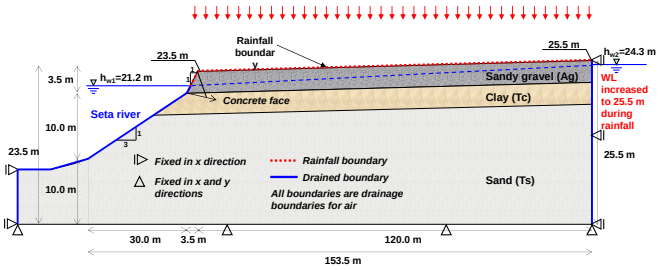

Figure 4 Cross section of the river embankment and its boundary conditions

The material parameters required by the constitutive model introduced here are listed in Table 1. These parameters can be determined from the boring tests such as N value and the parameters of materials similar to those soils. Detail of the parameters calculation can be obtained from Kimoto and Oka (2005). The parameters in Table 1 represent the three different soils found in the river embankment, namely, Sandy gravel (Ag), Clay (Tc), and Sand (Ts). The upper sandy gravel layer is a loose soil with N value of 2-4, it is about 3.0 m in height and it overlies on a clay layer about 4.0 m in height; the bottom of the embankment is composed of a stiff silty sand layer with N value of 50-60.

In order to study the effect of the rainfall infiltration and seepage flow into the unsaturated river embankment, the rainfall record and the water level measured from October 2nd to October 8th 2009 corresponding to the Seta River site is used in the simulation. As it was shown in Figure 3, the water level measured during this time at the mountain side was the maximum, reaching almost the top of the embankment. An enlargement of the rainfall record and the water measured at that time are shown together in Figure 5. The total precipitation was 106 mm, with a maximum hourly rainfall of 14 mm. According to the precipitation record, the rainfall was concentrated between the noon of October 7th to the morning of October 8th with a total rainfall of 97 mm (t=132 to t=152 h). During the simulation, the non-uniform rainfall is applied on the top and the slope of the river embankment, while the water level is increased on the right side (mountain side). The initial degree of saturation for the unsaturated soil (sandy gravel layer) is considered to be about 60%.

Table 1 Material parameters for Seta River simulations

Material Parameter	Sandy Gravel (Ag)	Clay (Tc)	Sand (Ts)
Viscoplastic parameter – m'	40	27	40
Viscoplastic parameter (1/s) – C_1	$1x10^{-15}$	$2x10^{-14}$	$1x10^{-20}$
Viscoplastic parameter (1/s) – C_2	$2x10^{-15}$	$2x10^{-13}$	$2x10^{-20}$
Stress ratio critical state – M^*_m	1.27	1.25	1.27
Compression index – λ	0.0804	0.4910	0.0804
Swelling index – κ	0.0090	0.0760	0.0090
Elastic shear modulus (kPa) – G_0	3000	23000	20000
Initial void ratio – e_0	0.344	1.23	0.535
Structural parameter – β	5	15	0
Structural parameter – $\sigma'_{maf}/\sigma'_{mai}$	0.60	0.579	0.60
Ver. water permeab. (m/s) – k^W_{sv}	**	$1x10^{-8}$	$1x10^{-6}$
Hor. water permeab. (m/s) – k^W_{sh}	**	$1x10^{-7}$	$1x10^{-5}$
Dry gas permeability (m/s) – k^G_s	$1x10^{-3}$	$1x10^{-3}$	$1x10^{-3}$
van Genuchten par. (1/kPa) – α	0.1	0.13	2
van Genuchten par. – n'	4	1.65	1.2
Suction parameter – S_I	0.2	0.2	0.2
Suction parameter – S_d	0.2	5	0.2
Minimum saturation – s_{min}	0	0	0
Maximum saturation – s_{max}	0.97	0.99	0.99
Shape parameter – a	3	3	3
Shape parameter – b	1	1	1

** The permeability of the sandy gravel layer depends on the simulation case

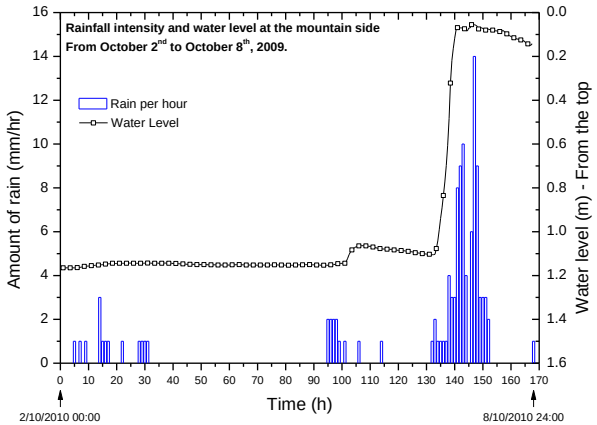

Figure 5 Cross section of the river embankment and its boundary conditions

At the site, it was observed that the deformation of the river embankments is localized at the river side, just below the concrete face that covers the surface of the slope. It is thought that this localized accumulation of deformation is triggered by a combined effect of the seepage flow due to the rainfall infiltration over the embankment surface, the seepage flow from the mountain side, and the difference in the permeabilities between the sandy gravel soil and the slope surface.

3.1.1 Simulation cases: Effect of Permeability

To see the effect of the permeabilities on the seepage flow velocity and the development of deformation in the unsaturated river embankment, different cases are analysed. The simulation cases are listed in Table 2. The analysed cases consist of different combinations of saturated permeabilities for the upper sandy gravel

layer and the slope surface. In Cases 1 to 4, both the saturated permeability of the sandy gravel and the saturated permeability of the slope surface are equal, and they are increased simultaneously, namely, $k^{W(G)}_{sv}$ = 1 x 10^{-6}, 3 x 10^{-6}, 6 x 10^{-6}, and 1 x 10^{-5} m/s. Cases 5 to 8 have been carried out in which a concrete face with smaller permeability than the top soil layer is assumed at the slope surface, This condition is similar to the current case at Seta river site; the saturated permeability for the sandy gravel is increased, i.e. $k^{W(G)}_{sv}$ = 1 x 10^{-6}, 3 x 10^{-6}, 6 x 10^{-6}, and 1 x 10^{-5} m/s, respectively, while the permeability of the slope surface is kept constant, i.e. $k^{W(S)}_{sv}$ = 1 x 10^{-7} m/s; in addition, the material of the slope surface is assumed to be an elastic material in order to simulate a concrete face over the slope of the embankment. For the elastic material the Elastic Young's modulus is considered to be E=1 GPa and the Poisson ratio ν=0.1.

Table 2 Saturated vertical permeabilities for the analysis

Case No.	Vertical Permeability	
	$k^{W(G)}_{sv}$ sandy gravel (m/s)	$k^{W(S)}_{sv}$ slope surface (m/s)
1	1x10^{-6}	1x10^{-6}
2	3x10^{-6}	3x10^{-6}
3	6x10^{-6}	6x10^{-6}
4	1x10^{-5}	1x10^{-5}
5	1x10^{-6}	1x10^{-7}
6	3x10^{-6}	1x10^{-7}
7	6x10^{-6}	1x10^{-7}
8	1x10^{-5}	1x10^{-7}

* The horizontal permeability is assumed to be 10 times the vertical permeability k^{W}_{sh}= 10 k^{W}_{sv}.

One of the greatest uncertainties concerning the study of rainfall infiltration and seepage flow lies on the field values of the saturated water permeability. Because the accumulation of deformation due to the seepage flow observed at the site is localized in the slope of the embankment (sandy gravel layer) and it is thought that this phenomenon is due to the water in infiltration; the results presented herein are based on the variation of the permeabilities for the upper layer, namely, sandy gravel layer, as well as the permeabilities of the slope surface. The permeabilities of the clay layer and the sand layer were kept constant. Different combinations among the permeabilities for the sandy gravel layer and for the slope of the embankment are used in order to find the permeability combinations that may lead to the localization of deformation at the slope of the embankment.

Cases 1 to 4 intend to evaluate the effect of the saturated water permeability on a homogeneous soil. Comparison of the horizontal hydraulic gradient distributions near the slope of the embankment at the time t=151 h for these cases is presented in Figure 6. This figure shows that the horizontal hydraulic gradient is very similar among the four cases, regardless of the permeability. Maximum values are obtained at the middle of the slope surface, immediately above the river water table. Comparison of the distributions of accumulated viscoplastic shear strain for these cases at the time t=151 h is shown in Figure 7. It is shown that the accumulation of viscoplastic shear strain is generated on the slope of the embankment immediately above the water level of the river. None of the cases show a large development of deformation on the slope of the embankment; however, a small accumulation of viscoplastic shear strain is evident above the water level near the slope surface. This can be attributed to the large hydraulic gradients presented on the surface of the slope above the water level. It can be said that due to homogeneity of the upper layer, the water can flow easily toward the river side avoiding the increase of the pore water pressure inside the embankment.

Cases 5 to 8 have been carried out in which a concrete face with small permeability is assumed at the slope surface. This is similar to the case found at Seta River site. Figure 8 shows the comparison of the distribution of the horizontal hydraulic gradient after the major rainfall (t=151 h) for Cases 5 to 8, respectively. Larger gradients are obtained for the cases with the concrete face; it suggests a large accumulation of water and the generation of pore water pressures at the back of the concrete face.

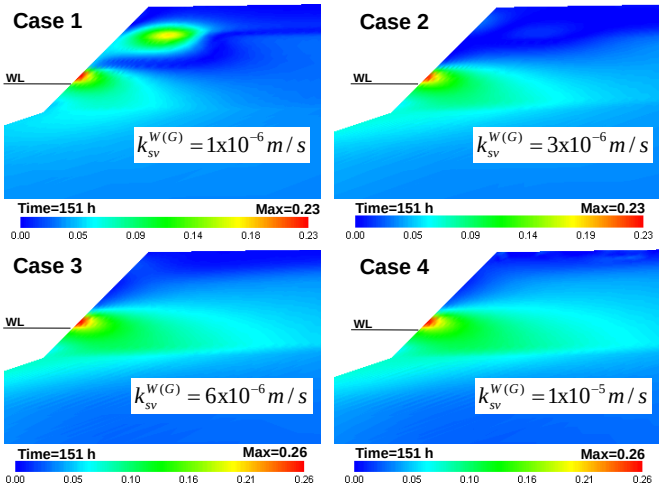

Figure 6 Distribution of the horizontal hydraulic gradient Cases 1 to 4 (t=151h)

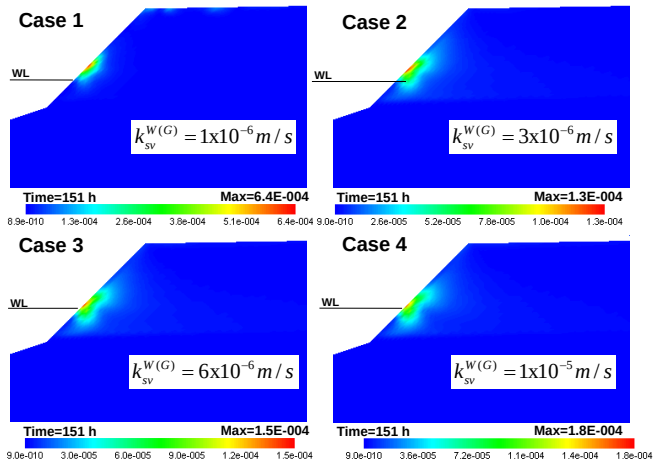

Figure 7 Distribution of the viscoplastic shear strain. Cases 1 to 4 (t=151h).

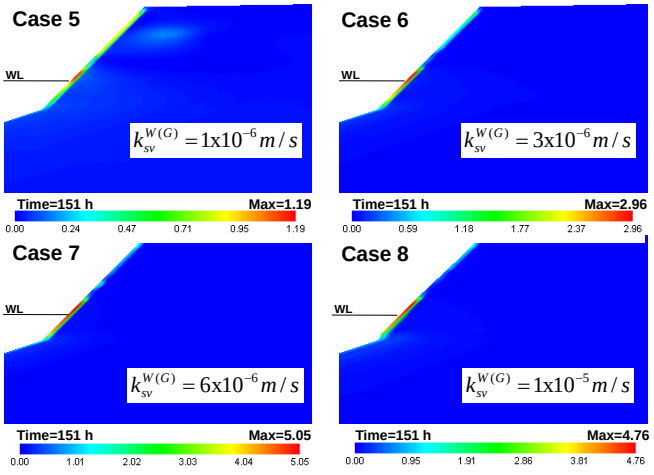

Figure 8 Distribution of the horizontal hydraulic gradient Cases 5 to 8 (t=151h)

Figure 9 presents the comparison of the distribution of viscoplastic shear strain for the cases 5 to 8 at the time t=151 h. This figure shows that the accumulation of viscoplastic shear strain is localized below the concrete face. This result is very similar to the

field observation, where a large deformation is presented below the concrete face in the embankment. Cases 5 to 7 show that the accumulated viscoplastic strains, after the major rainfall, are smaller; however, in Case 8, a large amount of accumulated viscoplastic strain (up to 49%) is generated. The water accumulated inside the embankment resulted in the accumulation of deformation of the soil on the back of the concrete face. Comparison of Figures 8 and 9 shows that, the localization of deformation below the concrete face is related to the hydraulic gradient and the permeabilities of the soil layer.

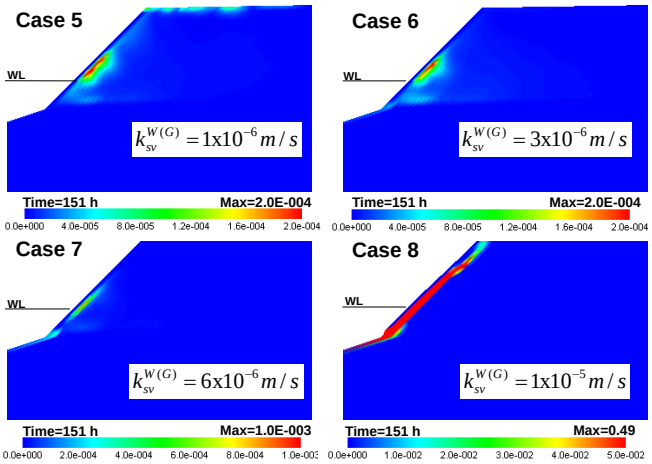

Figure 9 Distribution of the viscoplastic shear strain Cases 5 to 8 (t=151h)

By comparing the results of Cases 1 to 8 (Figures 6 to 9), it is possible to see that the effect of the permeability of the slope surface of a river embankment on its local instability is very significant. Larger hydraulic gradients and accumulated viscoplastic shear strains are obtained in the cases where the permeability of the slope surface is smaller compared to the permeability of the soil layer. It could be explained by the accumulation of the water behind the slope surface owing to the impediment of the water flow; as a result, larger pore water pressures and hydraulic gradients are generated at the back of the slope that may induce erosion. It suggests that some geotechnical measures to avoid the rainfall infiltration into the slopes, such as concrete faces and cement-soil mixtures, can be harmful for the local stability of the embankments if they are not accompanied by additional measures to reduce the water levels generated by the accumulation of water during the rainfall in infiltration. It supports the importance of the subsurface drainage of the soil structures in the improvement of their local and general stability.

3.1.2 Simulation cases: Effect of Horizontal Drains

In the practical geotechnical problems, if a free drainage boundary condition prevails at the surface of an embankment, the excess of water resulting from the water infiltration drains out freely avoiding the increase of the water table and the increase of the pore water pressure (Cases 1 to 4). However, if the water cannot flow out easily, it accumulates inside the embankment increasing the pore water pressure. Cases 5 to 8 showed that due to the rainfall infiltration and seepage flow, the water table rose within the river embankment and the pore water pressure increases. Moreover, once the pore water pressure develops at the back of the slope of the embankment, a highly unstable zone is developed in this area and the local failure occurs. It is evident that this problem could trigger larger instability zones due to the retrogressive advance in time of the erosion endangering the soil structure and inducing its global instability.

To overcome this problem it is convenient to allow the soil structure to dissipate the pore water pressure generated due to the build-up of the water table. To do that, subsurface drainage is recommended. Horizontal drains is one of the most common methods used for the subsurface drainage and it has been proved to be effective in preventing the development of pore water pressures due to the rainfall infiltration and seepage flow (e.g. Cai et al., 1998; Rahardjo et al., 2003; Ghiassian and Ghareh, 2008).

To show the effectiveness of the use of horizontal drains in the drainage of the excess of water generated inside the Seta River embankment, the same case in which the larger horizontal hydraulic gradients and larger deformations were presented (Cases 8) is simulated by using horizontal drains. This simulation is referred as Case 9. The same parameters listed in Table 1 are used; the location of the horizontal drains considered in the simulations is shown in Figure 10. Six rows of 3 m long horizontal drains spaced every 0.5 m are considered.

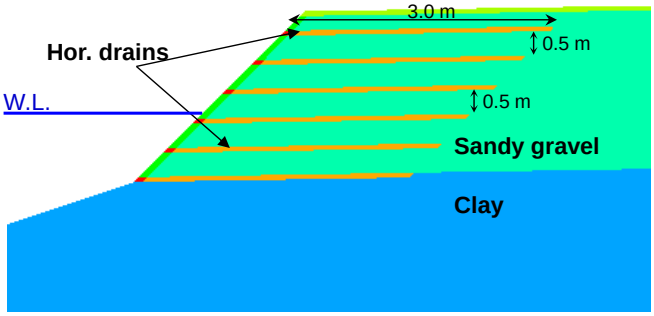

Figure 10 Location of the horizontal drains on the river embankment

The horizontal drain is introduced in the simulation as a drained boundary line. Each horizontal drain is evaluated according to its location and the present pore water pressure at the nodes as follows:

- In the case the drain nodes are located below the water level, i.e., saturated zone: The pore water pressures at the nodes are adjusted to the pore water pressure calculated according the water level of the river. Consequently, the excess of water is drained out and there is not flow of water from the river into the embankment.
- In the case the drain nodes are located above the water level, i.e., unsaturated zone: If the pore water pressures at the nodes are negative (suction), the node is treated as a normal node; as a result, the excess of water moves throughout the embankment as if the drains were not installed. Conversely, if the pore water pressure at the nodes is positive, the pore water pressure at the drain nodes is specified as a zero value. Therefore, the excess of water is drained out.

The drain nodes evaluated by the above boundary conditions allow the water to be drained out only in the case the surrounding soil is saturated.

The results of the distribution of the saturation at time t=151 h for the case without drains, namely, Case 8, and the case with drains, namely, Case 9, are shown comparatively in Figure 11. In these cases the same saturated water permeability for the sandy gravel layer is considered ($k^{W(G)}_{sv}$ = 1.0 x 10^{-5} m/s). When the numerical results are compared it is clearly shown by Case 9 that the installation of the horizontal drains considerably reduces the saturation and accumulation of the infiltrated water in the upper part of the embankment.

A comparison of the magnitude of the water velocity vectors for the same cases described above at the time t=151 h is shown in Figure 12. Comparing the results, the analysis without drains shows a vertical water flow due to the rainfall infiltration at the top of the embankment, nevertheless, the direction of the flow changes rapidly to be horizontal toward the slope of the river embankment. In contrast, in the analysis with horizontal drains, it is observed that the water flow have a dominant vertical direction toward the drains where the infiltrated water can be drained out. The water flow direction shows that the drains located at the bottom of the river embankment attract both the water due to the rainfall infiltration and

the seepage flow from the mountain side; it avoids the build-up of the water table at the river side.

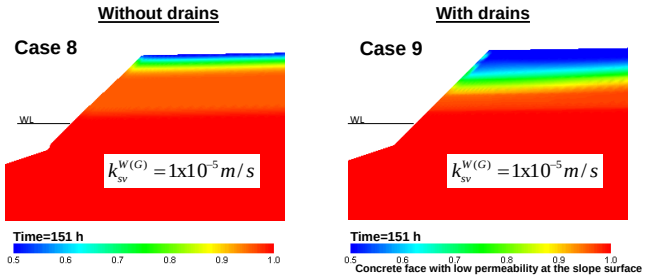

Figure 11 Distribution of saturation: Cases 8 and 9

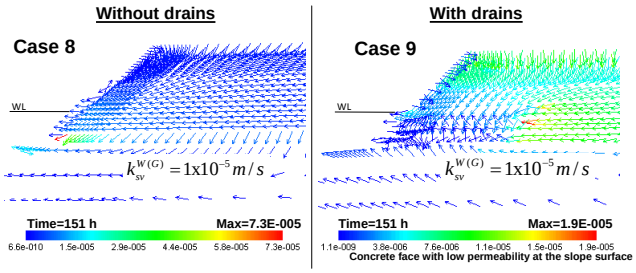

Figure 12 Distribution of water velocity vectors: Cases 8 and 9

In order to investigate the effect of the horizontal drains on the strain localization due to the rainfall infiltration and seepage flow, the distribution of the viscoplastic shear strain at time t=151 h for the case with drains is plotted together with that obtained for the case without drains in Figure 13. As shown on the left side of Figure 13, the accumulation of the viscoplastic shear strains for the case without drains is located all around the back of the concrete face. The strain accumulation is due to the increase of the water pressure at the back of the slope. For the analysis performed with the horizontal drains, it is seen that the accumulation of the strains disappear at the slope of the embankment; in addition, only small accumulations of irrecoverable deformation are presented inside the river embankment (maximum values around $4.0x10^{-5}$). It corroborates the effectiveness of the horizontal drains in avoiding the accumulation of deformation and the instability of the river embankments triggered by large seepage pressures that can be generated at the river sides due to the rainfall infiltration processes.

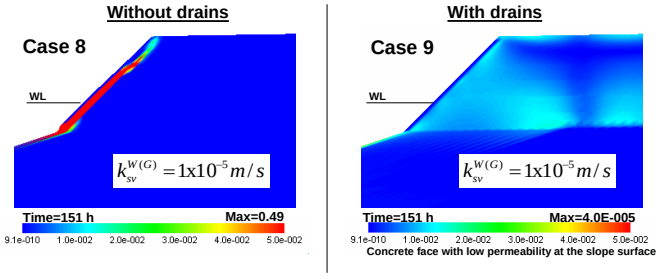

Figure 13 Distribution of the viscoplastic shear strain: Cases 8 and 9

3.1.3 Simulation cases: Effect of Compaction

One of the main parameters to determine the quality of the construction of the soil structures is the degree of compaction. Soil structures with larger degrees of compaction are expected to be more stable than those with smaller degrees of compaction. Larger degrees of compaction are associated with larger shear modulus and smaller development of strains. During the construction of embankments, however, it is very difficult to attain the compaction near the slope surface. This is because at the border of the embankments, the soil is unconfined and the compaction is hard to be achieved. Therefore, any river embankment with a lack of compaction at the river side could develop larger deformation and consequently a more rapid failure during the seepage infiltration. This deformation, could in turn, lead to the damage or nearby structures.

This section addresses the problem of large deformation in the river embankments due to the low compaction of the soil close to the river side. The influences of both the rainfall and the seepage flow are considered. Four cases are analysed to show the effect of compaction on the development and the localization of strains, namely, cases 8, 10, 11, and 12. Case 8 in Table 3 is selected as the reference case. To simulate a material with smaller degree of compaction, the initial elastic shear modulus G_0 is decreased, while the viscoplastic parameters C_1 and C_2 are increased for the soil within the first three meters of the sandy gravel layer as shown schematically in Figure 14. The remaining parameters are the same listed previously in Table 1.

Table 3 Material parameters for the study of the compaction effect

Material parameter		Cases			
		8	10	11	12
Initial Elastic Shear Modulus (kPa)	G_0	3000	2300	1600	900
Viscoplastic parameter (1/s)	C_1	$1x10^{-15}$	$1x10^{-13}$	$1x10^{-11}$	$1x10^{-9}$
Viscoplastic parameter (1/s)	C_2	$2x10^{-15}$	$2x10^{-13}$	$2x10^{-11}$	$2x10^{-9}$

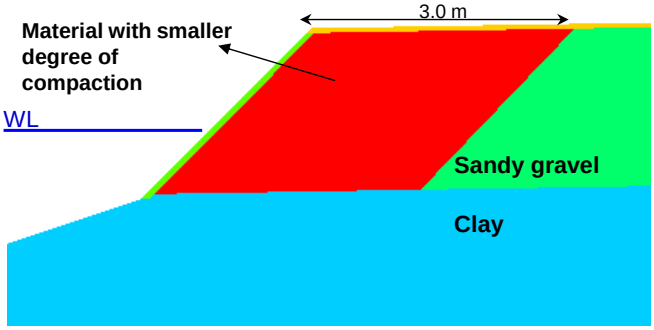

Figure 14 Location of the low compacted area

Comparison of the viscoplastic shear strain distributions, corresponding to the four cases, and for a rainfall infiltration time equal to 147.6 h is shown in Figure 15. The time t=147.6 h is chosen for the comparison because it is the time at which the simulation for Case 12 is numerically unstable due to the divergence of the deformation. It can be seen that a large amount of viscoplastic shear strain is generated in the sandy gravel layer below the concrete face

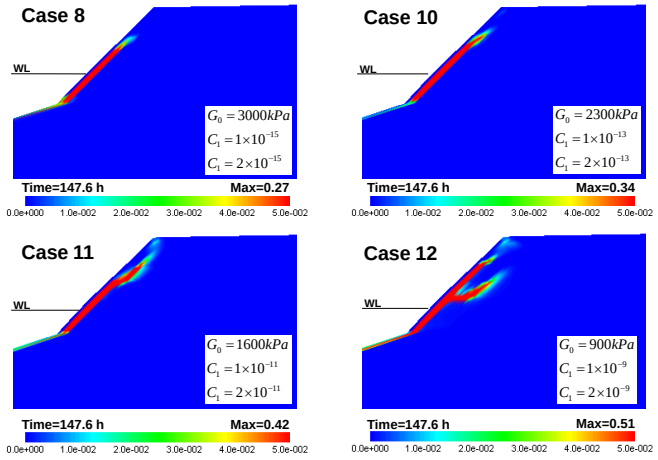

Figure 15 Distribution of the viscoplastic shear strain: Cases 8,10, 11, and 12

on the slope at the river side. This large strain extends from the bottom of the slope, and then progresses upward to the crest of the river embankment. By comparing the results of the analyses, we can observe that the viscoplastic shear strain increases as the material becomes weaker (smaller initial shear modulus and larger viscoplastic parameters, Cases 8, 10, 11 and, 12, respectively). The largest viscoplastic shear strain is obtained for case 12 (γ^{yp}=51%), which also corresponds to the largest shear zone. In this case, a second shear zone develops and progresses as a curve starting from the middle high of the slope of the embankment, which extends farther toward the upper part of the embankment.

3.2 Case B: S River - Japan

Torrential rains usually lead to the increase of the water level of the rivers triggering the failure of the river dike embankments due to seepage flow and overflow. In order to study the effect of the water infiltration due to the rise of the water level of the rivers on the river dikes, an experiment in the field has been performed. In the experiment rainfall intensity is applied on the surface of the river dike while the water level is increased and decreased to observe the effect of the seepage flow on the generation of pore water pressure and on the deformation of the embankment.

The cross section, the finite element mesh, and the boundary conditions for the simulation of the rainfall infiltration and seepage flow into the unsaturated river dike are shown in Figure 16. The top of the river embankment is 4.0 m wide. The right and the left slopes of the embankment have a gradient about 1V:2H. The height of the embankment at the right side is 3.14 m and at the left side 2.3 m. The bottom of the embankment is 15.0 m wide.

The foundation of the embankment is fixed at the bottom in both horizontal and vertical directions, the laterals boundaries are fixed only in horizontal direction. The water level in the soil is assumed to be located at the right side toe of the river dike (z=2.5 m). The unsaturated embankment is considered to have a constant initial saturation equal to s=0.80, i.e., the initial negative pore water pressure is assumed to be constant. The flux of air is allowed for the entire boundaries and the initial air pressure, P^G_i, is assumed to be zero. An impermeable boundary is assigned to the bottom of the soil foundation; for the lateral sides and the right top of the embankment foundation, the boundary is considered to be permeable. The right slope of the embankment is considered to be either a rainfall boundary if the water level is below the nodes or a drained boundary if the raising water reaches the nodes. Similarly, the left slope of the embankment and the left of the embankment foundation are considered to be either a rainfall boundary if the soil is unsaturated or a drained boundary in the case the pore water pressure becomes positive due to the seepage from the right side of the embankment. The top surface of the embankment is considered as a rainfall boundary.

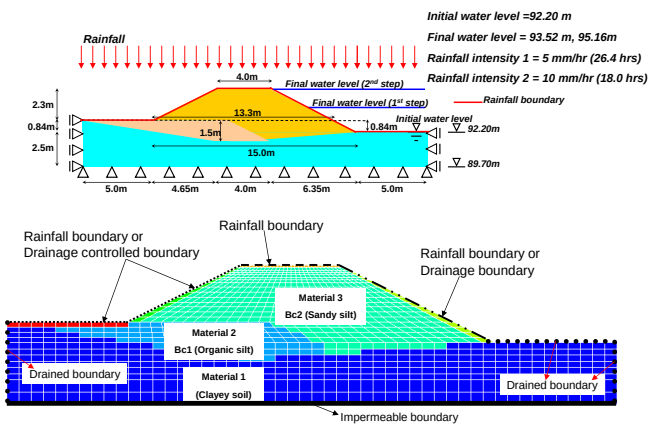

Figure 16 Cross section of the river embankment, element discretization, and boundary conditions

The river embankment is composed of three materials as shown schematically in Figure 16. These materials are considered to be elasto-viscoplastic materials. The same constitutive parameters are used for the three materials, except that the saturated water permeabilities of the Materials 2 (Bc1) and 3 (Bc2), are assumed to be different according the experimental tests. Bc1 indicates the middle stratum and it corresponds to organic silt, and Bc2 indicates the upper stratum and it corresponds to sandy silt, respectively. These soil layers overlie on a soil foundation composed of clayey soil (Material 1). The material parameters required for the simulation are listed in Table 4. These parameters belong to Material 3, which is the material directly affected by the infiltration process. For simplicity, these parameters are also used to represent the foundation soils found in the river embankment.

Table 4 Material parameters for the S River simulations

Material Parameter	
Viscoplastic parameter – m'	23
Viscoplastic parameter (1/s) – C_1	$1x10^{-8}$
Viscoplastic parameter (1/s) – C_2	$1x10^{-8}$
Stress ratio at critical state – M^*_m	0.947
Compression index – λ	0.03
Swelling index – κ	0.002
Elastic shear modulus (kPa) – G_0	28700
Initial void ratio – e_0	1.50
Structural parameter – β	0
Structural parameter – $\sigma'_{map}/\sigma'_{mai}$	1.0
Ver. water permeab. (m/s) – k^W_{sv}	**
Hor. water permeab. (m/s) – k^W_{sh}	**
Dry gas permeability (m/s) – k^G_s	$1x10^{-3}$
van Genuchten par. (1/kPa) – α	0.1
van Genuchten par. – n'	2
Suction parameter – S_l	0.2
Suction parameter – S_d	0.25
Minimum saturation – s_{min}	0
Maximum saturation – s_{max}	0.99
Shape parameter – a	3
Shape parameter – b	1

** The permeability is variable, which depends on the soil layer and the simulation case

The configuration of the experiment is shown schematically in Figure 17. In the experiment two lateral and one longitudinal sheet piles were used to make a water tank in order to control the level of the water at the right side of the river embankment. The distant between the lateral sheet piles is 15.0 m, while the longitudinal sheet pile was located 4.0 from the toe of the embankment. The height of the sheet piles is 4.0 m measured from the soil foundation. To apply constant rainfall intensity, various perforated pipes located about 4.0 meters from the toe of the embankment were used. The field experiment was performed by both artificial rainfall and seepage flow from the rise of the water level at the right side of the embankment.

Figure 18 shows the rainfall pattern and the right water level-time histories during the experiment program. For the rainfall, this figure indicates that the first rainfall equal to 5mm/h is applied during the times t=0 h and t=26.4 h and the second rainfall equal to 10mm/h is applied between the times t=26.4 and t=44.4 h. The total amount of rainfall applied to the embankment was 312 mm. For the water level, it is possible to see during the experiment that the water level at the right side of the embankment started to be increased at the time t=34.5 h, after 7.9 h the water level reached a height equal to 93.52 m and remained constant for 2 h; at the time t=44.4 h the water level decreased in 2.7 h to its initial water level and it was kept constant for 38.9 h. At the time t=86.0 h the water level started to be increased for 17.7 h until the height of 95.16 m was reached at the time t=103.7 h and it remained constant for 48.0 h. Finally, at

the time t=151.7 h the water level started to be decreased to its initial level in 6 h.

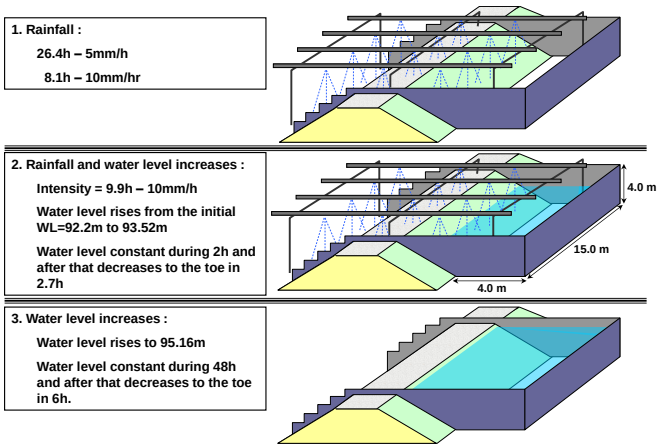

Figure 17 Sketch of the experimental configuration

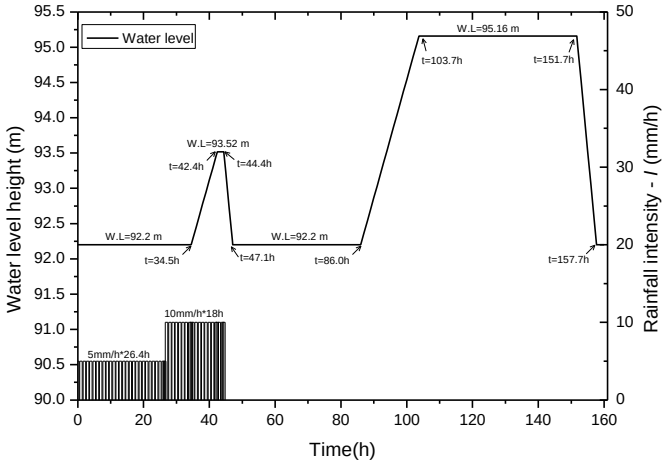

Figure 18 Rainfall and water level histories used for the experiment

3.2.1 Simulation cases: Effect of Permeability

As mentioned before, one of the greatest uncertainties concerning the study of rainfall infiltration and seepage flow lies on the field values of the saturated water permeability. Figure 19 shows a summary of the experimental results for the saturated permeabilities obtained by the laboratory tests, the field measurements, and those estimated by the gradation of the soils. The results are shown for materials 2 and 3, respectively. From Figure 19 it can be seen that the permeabilities obtained by the laboratory tests and those obtained by field measurements significantly differ among them. In general, the laboratory permeabilities are much smaller than those obtained by the field measurements. These differences can be explained by the heterogeneity of the material and the disturbance of the soil samples during the laboratory tests. This figure also shows the average saturated permeabilities which were calculated by averaging all the results. Because of the high variability of the results obtained for the permeabilities of the soils, it is necessary to perform a parametric analysis to seek for the permeability values that can represent the soils. Therefore, in order to compare the results of the water levels obtained in the simulation with the results of the field measurements, different permeabilities were used for the layers Bc1 and Bc2.

Five cases are considered in the parametric analysis. These cases consist mainly of the combination of different saturated permeabilities for the middle and the upper layers. The range of the permeabilities used for the analysis varies from the average permeabilities (Bc1: k^{W}_{sv} =1.5 x 10^{-7} m/s, Bc2: k^{W}_{sv} =4.2 x 10^{-7} m/s) to two times the average permeabilities. The simulation program is outlined in Table 5. The horizontal permeability is considered to be 10 times the vertical permeability for Cases 1 to 3 and 7.5 times the vertical permeability for Cases 4 and 5. The initial water level (minimal water level in the simulations) is assumed to be 92.2 m, except for Case 5 where it is assumed to be 91.9 m.

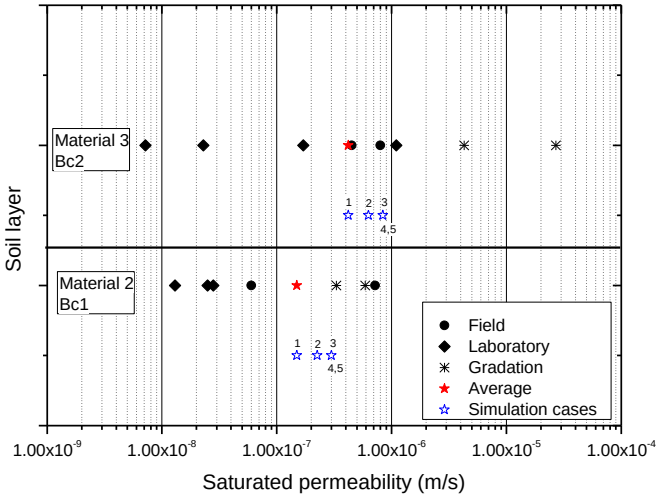

Figure 19 Summary of the measured saturated water permeabilities

Table 5 Saturated water permeabilities for the simulated cases

Case No.	k^{W}_{sv} (m/s) Layer Bc1	k^{W}_{sv} (m/s) Layer Bc2	k^{W}_{sh} (m/s)	Initial WL (m)
1	$1.50\text{x}10^{-7}$	$4.20\text{x}10^{-7}$	$10k^{W}_{sv}$	92.2
2	$2.25\text{x}10^{-7}$	$6.30\text{x}10^{-7}$	$10k^{W}_{sv}$	92.2
3	$3.00\text{x}10^{-7}$	$8.40\text{x}10^{-7}$	$10k^{W}_{sv}$	92.2
4	$3.00\text{x}10^{-7}$	$8.40\text{x}10^{-7}$	$7.5k^{W}_{sv}$	92.2
5	$3.00\text{x}10^{-7}$	$8.40\text{x}10^{-7}$	$7.5k^{W}_{sv}$	91.9

During the test, the positive pore water pressure response was monitored by installing pore water pressure sensors within the river embankment. A total of 14 sensors were placed at different elevations and they were located closer to the toe of the embankment as shown schematically in Figure 20. The sensors were connected to a computer-based data acquisition system. The pore water pressures measured by the sensors were automatically converted to water heights. In the sensor labels presented in Figure 20, the number indicates the depth of the location of the sensor projected vertically from the surface of the river embankment.

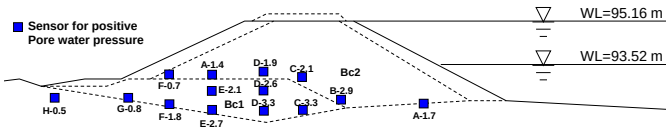

Figure 20 Sensor location for the measurement of pore water pressure

Figure 21 shows the measured results of the change of the water levels (change in positive pore water pressures) at the sensor locations in Figure 20. This graph shows that when the rainfall was applied, only a small accumulation of water is observed at the bottom of the embankment. However, when the water level at the right side of the embankment was increased to the heights of 93.52 m and 95.16 m, the water infiltrated into the soil increasing the pore water pressures at the bottom of the embankment. The water levels are higher at the right side of the embankment and gradually decrease toward the left side of the embankment.

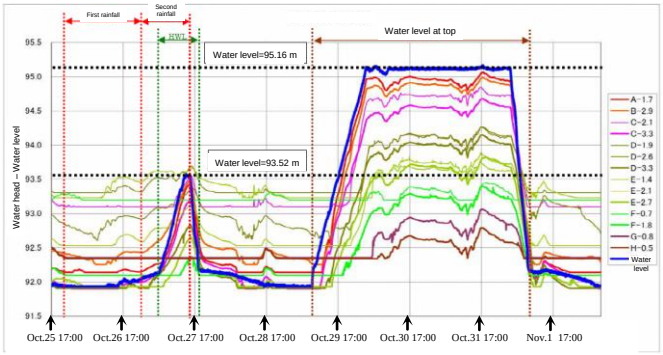

Figure 21 History of the measured water levels

The numerical results of the saturation distribution when the water level is constant at the height h=93.52 m (t=44.4 h), the water level starts to increase at 86.0 h to the height h=95.16 m, the water level is at the crown of the embankment at t=103.7 h, and before the water level decreased at t=151.7 h are shown together in Figure 22. Figure 22(a) shows the saturation distribution when the water level on the river side reaches the height h=93.52 m and remained constant for 2 h. A saturated zone is observed at the right side of the embankment due to the seepage flow infiltrated within the soil from the river side. It is also observed that most of the embankment is unsaturated; however, its saturation increases due to the rainfall infiltration and the advance of the water front.

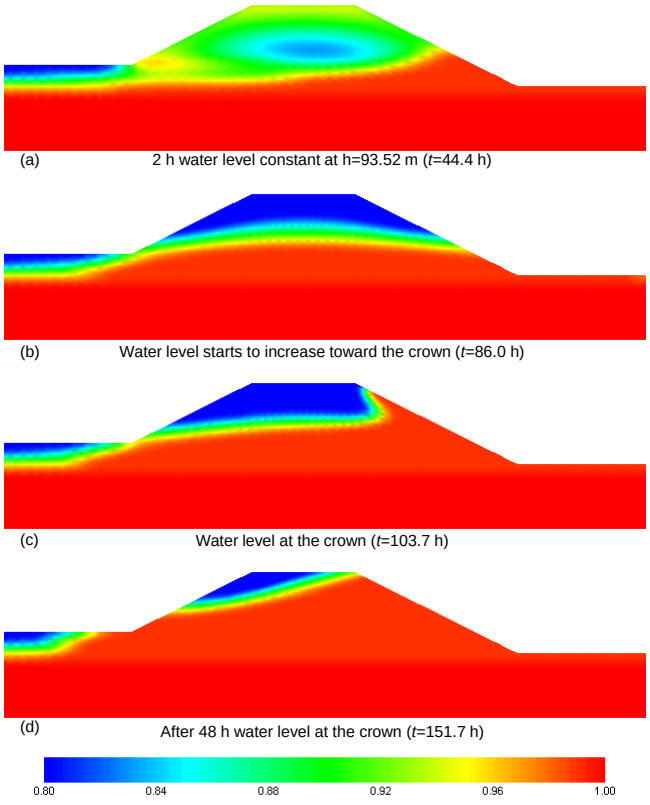

Figure 22 Distribution of saturation during the infiltration process

The saturation distribution just before the water level is increased to the height h=95.16 m is presented in Figure 22(b), the results shows the accumulation of the water at the bottom of the embankment due to the rainfall infiltration and the seepage flow. Figures 22(c)-(d) show the saturation distributions when the water level reached the crest of the embankment and after it remained constant for 48 h at that level, respectively. It can be seen that, after 48 h the water level was at the crest of the embankment, most of the soil within the embankment became saturated due to the water infiltration from the river side.

Figures 23-25 shows the simulation results of the water levels within the elapsed time for the Cases 1, 3 and, 5, respectively. The position of the soil elements in the mesh is approximately the same position of the sensors within the embankment (Figure 20). From this figure, it is possible to see that the water levels within the embankment (positive pore water pressures) increase meanly when the water level increases at the right side of the embankment. The results do not show a significant effect of the rainfall at the beginning of the simulation on the increase of the water level. This is consistent with the measurements results by the positive pore water pressure sensors installed within the embankment. It can be explained by the low permeability of the soil which does not allow the water to move rapidly downward, toward the water table.

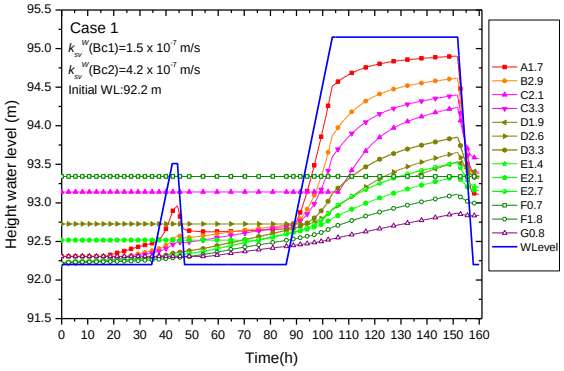

Figure 23 Histories of the increase of water level at the sensors location (Case 1)

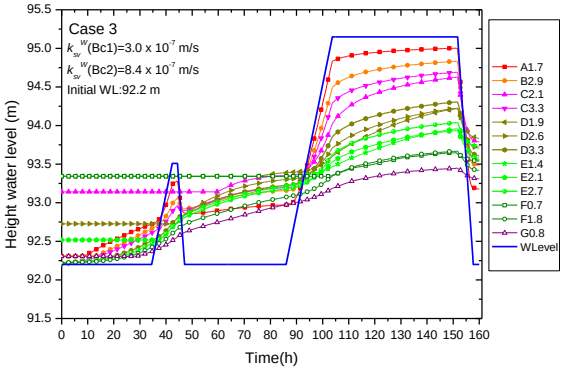

Figure 24 Histories of the increase of water level at the sensors location (Case 3)

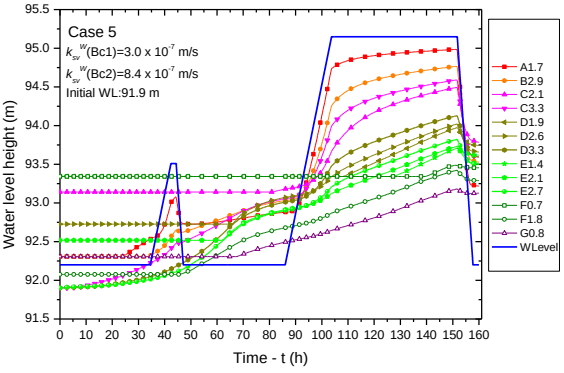

Figure 25 Histories of the increase of water level at the sensors location (Case 5)

From Figures 23 to 25, it was observed that the case with the permeability combinations and the initial water level that lead to better results when compared with the field measurements corresponds to Case 5. Case 5 show a better agreement in the increase of the water levels inside the slope when the water level is increased at the right side of the river embankment. The comparison

with Figure 21 shows that the water levels in the simulation increase slower than the water levels measured in the field. Nevertheless, the general trend of the increase of the water level within the embankment and the final results obtained by the simulation show a good agreement. It was not possible to simulate the rapid build-up of the ground water table as well as the rapid dissipation of the pore water pressure at the left side of the embankment during the field test. These differences can be explained by the heterogeneity of the material which plays an important role on the permeability function of the soil and on the flow paths for the infiltrated water. It suggests that more accurate information about the permeabilities of the soil, the soil-water characteristic curves, and their hysteretic behaviour during the wetting and drying paths are necessary to improve the simulation results. It emphasizes the significance of the experimental tests and field data related to infiltration on unsaturated soils in the improvement of the numerical models to understand the complex response of unsaturated soils.

Figure 26 shows the distribution of the viscoplastic shear strain. From this figure it is seen that the viscoplastic shear strain develops prominently at the right side of the embankment during the rainfall infiltration. The viscoplastic strain reaches a maximum value of 9.8% after 34.5 h of rainfall infiltration (Figure 26(b)). Figures 26(c) and (d) show the viscoplastic shear strain attained at the time intervals t=103.7 h and t=151.7 h, respectively. These figures show that the accumulation of the deformation at the right side of the embankment increases to a maximum viscoplastic shear strain of 12.1%. It can be said, in this case, that the accumulated viscoplastic shear strain at the toe of the embankment is mainly due to the seepage flow at the right slope of the embankment.

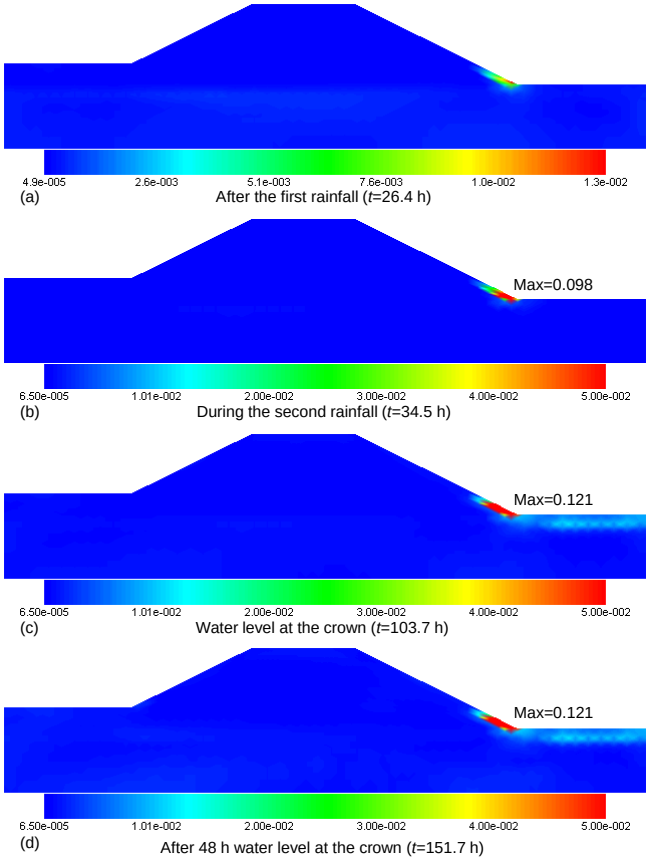

Figure 26 Distribution of viscoplastic shear strain during the infiltration process

4. CONCLUSION

In this paper, two-dimensional numerical simulations of two case studies of unsaturated river embankments subjected to rainfall infiltration and seepage flow were carried out. The distribution of the pore water pressures and the pattern of deformations were investigated. In the analyses, the mechanism of the surface deformation and the strain localization on the embankment surface at the river side were discussed mainly with respect to the water permeability of the soil. From the numerical results, it was found that the deformation of the embankment significantly depends on the water permeability of the soil and it is localized on the slope surface at the river side. The larger the saturated water permeability of the soil, the larger the velocity of the seepage flow and the larger the deformation on the surface of the river embankment.

In the Seta River case, different simulations were performed to study the effects of the permeability, the subsurface drainage, and the degree of compaction on the deformation of unsaturated river embankments. The results of the analyses of the river embankment with smaller permeabilities at the slope surface (e.g., concrete face) showed that larger hydraulic gradients and larger accumulated viscoplastic shear strains are obtained at the back of the slope surface. This deformation was induced by the accumulation of the water behind the slope surface owing to the impediment of the water to flow toward the river. However, the deformation of the slope surface was avoided when the horizontal drains were used in the simulations. The horizontal drains showed to be very effective in avoiding the accumulation of deformation and the local instability of the river embankments caused by the large seepage pressure presented at the river sides during the infiltration processes. From the simulations of the embankments with different compaction levels, larger deformations were obtained for the soil with smaller degrees of compaction.

In the case of S River, a comparison between the simulation results for the water levels within the embankment and the field measurement values yields a good agreement and indicates that the calculation method adopted here can effectively be used to study the practical seepage deformation coupled problems on unsaturated soils. However, there is a need of more field and experimental data related to the hydraulic and deformation behaviour of unsaturated soils in order to improve the numerical model and the simulation processes.

5. ACKNOWLEDGMENT

This study has been performed as a part of the Project on monitoring of the Ground Water in the River Levee supported by Kinki Regional Development Bureau, Japan (2008–2009). The authors would like to express sincere thanks to Japan Institute of Construction Engineering for giving us a permission of data of the seepage flow of test embankment.

6. REFERENCES

Alonso, E.E., Gens, A., and Delahaye, C.H. (2003). "Influence of rainfall on the deformation and stability of a slope in overconsolidated clays: a case study". Hydrogeology Journal, 11, pp174-192.

Au, S.W.C. (1993). "Rainfall and slope failure in Hong Kong". Engineering Geology, 36, pp141-147.

Au, S.W.C. (1998). "Rain-induced slope instability in Hong Kong". Engineering Geology, 51, pp1-36.

Biot, M.A. (1941). "Three-dimensional theory of consolidation". Journal of Applied Physics, 12(2), pp155-164.

Biot, M.A. (1962). "Mechanics of deformation and acoustic propagation in porous media". Journal of Applied Physics, 33(4), pp1482-1498.

Boer, R.D. (1998). "Theory of porous media - past and present". Zeitschrift fur Angewandte Mathematik und Mechanik, 78(7), pp441-466.

Cai, F., and Ugai, K. (2004). "Numerical analysis of rainfall effects on slope stability", International Journal of Geomechanics, 4(2), pp69-78.

Cai, F., Ugai, K., Wakai, A., and Li, Q. (1998). "Effects of horizontal drains on slope stability under rainfall by three dimensional finite element analysis". Computers and Geotechnics, 23(4), pp255-275.

Chen, H., Dadson, S., and Chi, Y.G. (2006). "Recent rainfall-induced landslides and debris flow in Northern Taiwan". Geomorphology, 77, pp112-125.

Cho, S.E., and Lee, S.R. (2001). "Instability of unsaturated soil slopes due to infiltration". Computers and Geotechnics, 28, pp185-208.

Ehlers, W., Graf, T., and Amman, M. (2004). "Deformation and localization analysis of partially saturated soil". Computer Methods in Applied Mechanics and Engineering, 193, pp2885-2910.

Fung, Y.C., and Tong, P., (2001). "Plasticity: Classical and Computational Solid Mechanics". World Scientific, Singapore.

Ghiassian, H., and Ghareh, S. (2008). Stability of sandy slopes under seepage conditions, Landslides, 5, pp397-406.

Jommi, C. (2000). "Remarks on the constitutive modeling of unsaturated soil". Experimental evidence and Theoretical Approaches in Unsaturated Soils. pp. 139-153.

Kimoto, S., and Oka, F. (2005). "An elasto-viscoplastic model for clay considering destructuralization and consolidation analysis of unstable behavior". Soils and Foundations, 45(2), pp29-42.

Kimoto, S., Oka, F., and Fushita, T. (2010). "A chemo-thermo-mechanically coupled analysis of ground deformation induced by gas hydrate dissociation". International Journal of Mechanical Sciences, 52(2), pp365-376.

Kimoto, S., Oka, F., Fushita, T., and Fujiwaki, M. (2007). "A chemo-thermo-mechanically coupled numerical simulation of the subsurface ground deformations due to methane hydrate dissociation". Computer and Geotechnics, 34, pp216-228.

Matsushi, Y., Ayalew, L., Hattanji, T., and Matsukura, Y. (2006). "Mechanisms of shallow landslides on soil-mantled hillslopes with permeable and impermeable bedrocks in the Boso Peninsula, Japan". Geomorphology, 76, pp92-108.

Nakata, Y., Liu, D., Hyodo, M., Yoshimoto, N., and Kato, Y. (2010). "Numerical simulation of an expressway embankment slope failure". Unsaturated Soils, Theoretical and Numerical Advances in Unsaturated Soil Mechanics, pp719-724.

Nemat-Nasser, S. (2004). "Plasticity: A Treatise on Finite Deformation of Heterogeneous Inelastic Materials". Cambridge University Press, Cambridge.

Ng, C.W.W., and Shi, Q. (1998). "A numerical investigation of the stability of unsaturated soil slopes subjected to transient seepage". Computers and Geotechnics, 22(1), pp1-28.

Oka, F., Kimoto, S., Takada, N., and Higo, Y. (2009). "A multi-phase elasto-viscoplastic analysis of a unsaturated river embankment associated with seepage flow". Proceedings. of the International Symposium on Prediction and Simulation Methods for Geohazard Mitigation. pp127-132.

Oka, F., Kodaka, T., Kimoto, S., Kim, Y.-S., and Yamasaki, N. (2006). "An elastoviscoplastic model and multiphase coupled FE analysis for unsaturated soil". Proceedings of the fourth international conference on unsaturated soils. pp124-131.

Oka,F. and Kimoto,S. (2012). ”Computational modeling of multiphase geomaterials”. CRC press, Taylor & Francis Group, New York, London and Boca Raton.

Okada, K., and Sugiyama, T. (1994). "A risk estimation method of railway embankment collapse due to heavy rainfall". Structural Safety, 14, pp131-150.

Rahardjo, H., Hritzuk, K.J., Leong, E.C., and Rezaur, R.B. (2003). "Effectiveness of horizontal drains for slope stability". Engineering Geology, 69, pp295-308.

Rahardjo, H., Ong, T.H., Rezaur, R.B., and Leong, E.C. (2007). "Factors controlling instability of homogeneous soil slopes under rainfall". Journal of Geotechnical and Geoenvironmental Engineering, 133(12), pp1532-1543.

Terzaghi, K. (1943). "Theoretical soil mechanics". John Wiley & Sons.

Tsaparas, I., Rahardjo, H., Toll, D.G., and Leong, E.C. (2002). "Controlling parameters for rainfall-induced landslides". Computers and Geotechnics, 29, pp1-27.

Van Genuchten, M. Th. (1980). "A closed-form equation for predicting the hydraulic conductivity of unsaturated soils. Soil Science Society of America Journal, 44, pp892-899.

Yamagishi, H., Horimatsu, T., Kanno, T., and Hatamoto, M. (2004). "Recent landslides in Niigata Region, Japan". Proceedings of the 4th Asian Symposium on Engineering Geology and the Environment, Hong Kong, p7

Yamagishi, H., Watanabe, N., and Ayalew, L. (2005). "Heavy-rainfall induced landslides on july 13, 2004, in Niigata Region, Japan". Monitoring, Prediction and Mitigation of Water Related Disasters, p6.

Ye, G., Zhang, F., Yashima, A., Sumi, T., and Ikemura, T. (2005). "Numerical analyses on progressive failure of slope due to heavy rain with 2D and 3D FEM". Soils and Foundations, 45(2), pp1-15.

Yoshida, Y., Kuwano, J., and Kuwano, R. (1991). "Rain-induced slope failures caused by reduction in soil strength". Soils and Foundations, 31(4), pp187-193.